npj | 2D materials and applications

www.nature.com/npj2dmaterials

ARTICLE OPEN

Experimental and theoretical studies of native deep-level defects in transition metal dichalcogenides

Jun Young Kim[1,2,6]✉, Łukasz Gelczuk[3,4,6]✉, Maciej P. Polak[2], Daria Hlushchenko[4,5], Dane Morgan[2], Robert Kudrawiec[4,5]✉ and Izabela Szlufarska[2]✉

Transition metal dichalcogenides (TMDs), especially in two-dimensional (2D) form, exhibit many properties desirable for device applications. However, device performance can be hindered by the presence of defects. Here, we combine state of the art experimental and computational approaches to determine formation energies and charge transition levels of defects in bulk and 2D MX_2 (M = Mo or W; X = S, Se, or Te). We perform deep level transient spectroscopy (DLTS) measurements of bulk TMDs. Simultaneously, we calculate formation energies and defect levels of all native point defects, which enable identification of levels observed in DLTS and extend our calculations to vacancies in 2D TMDs, for which DLTS is challenging. We find that reduction of dimensionality of TMDs to 2D has a significant impact on defect properties. This finding may explain differences in optical properties of 2D TMDs synthesized with different methods and lays foundation for future developments of more efficient TMD-based devices.

npj 2D Materials and Applications (2022)6:75 ; https://doi.org/10.1038/s41699-022-00350-4

INTRODUCTION

Transition metal dichalcogenides (TMDs) have been extensively studied for device applications. In particular, the direct band gaps of two-dimensional (2D) TMDs and the tunability of band gaps have attracted great attention in the fields of electronics and optoelectronics applications. Specifically, 2D MX_2 (M = Mo or W; X = S, Se, or Te) are considered to be promising for a variety of electronic, photonic, energy and sensing device applications that are more efficient than cutting edge silicon-based devices[1–4]. Depending on their chemical compositions and structural configuration, TMDs can cover a wide range of band gaps through the proper selection of metal or chalcogen species. In addition, TMDs are easily combined with other 2D materials such as hexagonal boron nitride or graphene to form van der Waals (vdW) heterostructures, revealing unique properties such as large in-plane stability and enabling applications such as flexible electronics[5–8].

To critically assess TMDs for device applications, it is necessary to consider defects in these materials because a finite number of defects is always present and influences material properties and the performance of devices. For instance, Liu et al. reported enhanced mobility of MoS_2-based field effect transistors when MoS_2 is annealed in sulfur[9], and it was proposed that the improved device performance results from the removal of sulfur vacancies. In addition, when present in high concentration, defects play a crucial role in determining electrical properties of materials, since free charge carriers trapped at defect levels cause Fermi level pinning at contacts and control the type of doping[10–12]. Also, Qiu et al. reported that charge transport mechanism of MoS_2 in the low carrier density regime is caused by nearest-neighbor hopping through V_S-induced localized gap states[13]. Therefore, to properly design TMD-based applications, it is important to accurately determine the charge transition levels of defects in TMDs.

The charge transition levels of defects in TMDs have been studied experimentally[14–25] and computationally[10,11,26–30], mostly focusing on MoS_2. Among various defects, sulfur vacancy has been found to be the most stable intrinsic defect[14,26,27] in both bulk and 2D MoS_2, and computational studies have focused on the charge transition levels of sulfur vacancy[26–28]. For example, in a density functional theory (DFT) based study, Komsa et al.[27] reported the defect chemistry and the charge transition levels of native defects in bulk and 2D MoS_2, and they found that the charge transition levels of sulfur vacancy are similar in bulk and 2D MoS_2. More recently, Tan et al.[28] calculated the charge transition levels of sulfur vacancy in bulk and 2D MoS_2, utilizing the electrostatic correction for 2D systems developed by Freysoldt and Neugebauer[31,32], which is considered the most accurate electrostatic correction to date. However, none of the previous studies used a method that accurately describes the band gap to determine the charge transition levels, leading to difficulty in comparing with experimental charge transition levels, because experimental methods such as deep level transient spectroscopy (DLTS) provide information on charge transition levels referenced to the conduction band minimum (CBM), i.e., deep acceptors for *n*-type samples. Considering the importance of vdW interactions between layers of bulk TMDs, it is critical to carefully choose an approach that is capable of describing them well within DFT. Especially, since structural parameters such as lattice constants and vdW interactions play a key role in determining the electronic structure and charge transition levels, use of the most accurate approach is expected to be important. Recently, Tran et al. found that rev-vdW-DF2 functional is highly accurate for weakly bound solids including TMDs[33]. Overall, although theoretical charge transition levels

[1]Department of Electrical and Computer Engineering, University of Wisconsin–Madison, Madison, WI 53706, USA. [2]Department of Materials Science and Engineering, University of Wisconsin–Madison, Madison, WI 53706, USA. [3]Department of Nanometrology, Wroclaw University of Science and Technology, Janiszewskiego 11/17, Wroclaw 50-372, Poland. [4]Departament of Semiconductor Materials Engineering, Wroclaw University of Science and Technology, Wybrzeze Wyspianskiego 27, Wroclaw 50-370, Poland. [5]LUKASIEWICZ Research Network, PORT Polish Center for Technology Development, Stablowicka 147, 54-066 Wroclaw, Poland. [6]These authors contributed equally: Jun Young Kim, Łukasz Gelczuk. ✉email: junyoungkim729@gmail.com; lukasz.gelczuk@pwr.edu.pl; robert.kudrawiec@pwr.edu.pl; szlufarska@wisc.edu

have been reported, as we will show later, there have been discrepancies in the reported values and in many cases the predictions have not been validated experimentally. There is thus still room for improving the accuracy and reliability by combining the state-of-the-art methods: selection of functional, electrostatic correction, and use of correct band gap[27].

Experimental characterization of defects in TMDs refer mostly to intrinsic structural properties of MoS_2 at the atomic scale, studied by means of high-resolution transition electron microscopy (HRTEM)[13,14,26] or scanning tunneling microscopy (STM)[15–17,34,35]. However, very little attention has been paid to other promising TMDs, such as WSe_2, WS_2, $MoSe_2$, or $MoTe_2$. In recent years, there have been at most several reports presenting research into the atomic structure of defects in these materials[34–36]. Experimental structural investigations are often supported by first-principles calculations, which can help identify the nature of the defects. Indeed, systematic joint experimental-theoretical investigations have provided distinct evidence that sulfur vacancies exist in MoS_2 and introduce charge transition levels inside the band gap[13,14,26]. While STM is capable of studying both the structural and electronic properties of various types of defects on the surface of TMDs, TEM measurements can only visualize the defect structure and do not provide a direct access to the electronic properties of individual defects[17], i.e., their activation energy or capture cross-section. There is also distinct inconsistency on the defect types revealed from STM and TEM experiments, as well as discrepancy in signatures of defect-induced deep in-gap states from theoretical calculations[13,14,26]. These problems arise mostly from unclear differentiation of STM contrast between the metal and chalcogen sublattices and the complicated convolution of electronic and geometric structures[17], as well as very limited capability in detecting defects beneath the surface[25]. Therefore, optical spectroscopic techniques, e.g., Raman or photoluminescence (PL) spectroscopy are also widely used for defect characterization in 2D layered materials, such as graphene or TMDs[18–22]. Because the change of Raman features with increase of defect density is less sensitive in TMDs than in graphene, PL spectroscopy appears to be a more reliable and sensitive way to examine in-gap defect states in TMDs. For example, Tongay et al. found a subband gap emission peak in low-temperature PL spectra of monolayer MoS_2 after α-particle irradiation, which the authors attributed to the emission from the charge transition levels of sulfur vacancies[19]. Defect-related PL emissions were also observed in monolayer WSe_2[20] and WS_2[21,22] and attributed by the authors to the recombination of excitons bound to different types of native defects, most probably chalcogen vacancies. In the meantime, electrical characterization of defects has been limited, mainly due to the difficulties in getting good quality electrical contacts to 2D TMDs with reduced contact resistance[10,11,37]. However, recent years have brought significant progress towards high-quality electrical contacts, such as the use of metallic 2D materials as electrical contacts to semiconducting TMDs[37]. For example, in MoS_2/graphene heterojunction transistors, Kwak et al. found a deep donor level using the *I*–*V* measurement and estimated its origin to be related to intrinsic or extrinsic donor sources such as rhenium impurities or sulfur vacancies[23].

Despite many of the previous efforts in determining the charge transition levels of defects in TMDs, these transition levels are still experimentally unknown or there are significant discrepancies between individual reports. Moreover, the reported experimental results are mostly devoted to sulfur vacancies in MoS_2 and the issue of other types of native defects, e.g., interstitials, antisites, and/or impurities in other types of TMDs, is generally neglected. For better understanding and to increase usability of TMDs in device applications the type and the energy levels of defects should be well documented, as it has been done for conventional semiconductors. Much better compatibility between the theoretically predicted and experimentally determined deep energy levels of defects can be obtained from a direct measurement. DLTS method has the advantage over other techniques used to-date in that it fulfils almost all the requirements for a complete and direct characterization of deep centers and their correlation with device properties. In particular, the DLTS method can determine the activation energy of a deep level, as well as its capture cross-section and concentration. In addition, it can distinguish between traps and recombination centers, between point and extended defects (e.g., dislocations) or bulk and interface states. Optical methods such as photoluminescence (PL) can be applied only for those impurities for which radiative recombination is observed. Compared to DLTS, PL may allow in some cases for easier impurity identification, but it is more difficult for concentration measurements. Furthermore, PL has the advantage of being nondestructive, contactless method, which allows deep-level mapping on large area samples, but it also requires complex and very expensive instruments, i.e., laser, refrigerator, spectrometer, photon counting, and detection system. On the other hand, STEM or STM methods probe only small area samples, allowing direct observation of defects and estimation of their density but they fail in determining the exact energy level positions in the band gap. Nevertheless, in order to effectively identify defects revealed by DLTS, partial support by other experimental techniques and theoretical calculations is highly advisable. Unfortunately, it is technically challenging to apply DLTS to either bulk or 2D TMDs, owing to many known issues, such as good quality metal-semiconductor (m–s) junction, high leakage currents and low series resistance, or a sufficient width of the depletion region under the interface[10–12,24,25]. Good quality Schottky and ohmic contacts are crucial to performing any electrical characterization of semiconductor materials and for device applications. In the case of nonideal Schottky diodes or p-n junction, the device parasitic components, such as high series and contact resistances or leakage currents, can significantly affect the DLTS signal. For bulk semiconductors, good quality contacts can be obtained by standard metal deposition under moderate conditions, which limits the detrimental interaction of the deposited metal atoms with the underlying TMD crystal. However, in the case of atomically thin materials, standard metal deposition approaches may cause significant damage to the metal-2D semiconductor junction, by introducing interface defects. Defects at the interface lead to the “pinning effect” of the Fermi level, which in turn prevents modulation of the Schottky barrier height (SBH) with metal work function[38]. Therefore, in order to make clean contacts (i.e., free of defects) to 2D TMDs, it is recommended to use high-quality TMDs with low defect density, use metals with low vaporization temperatures, avoid highly reactive metals, or use very high vacuum conditions during metal deposition[39]. Another promising approach is to use a so-called vdW m–s junction in which atomically flat metallic contact is placed on top of the 2D semiconductor without direct chemical bonding. In this case, only weak vdW bonding exists at the interface that is generally free from any chemical disorder, interface electronic states, and Fermi level pinning[39,40].

We have recently reported a successful usage of DLTS method for direct probing of deep-level defects in bulk MoS_2 vdW crystal[24]. Standard DLTS temperature spectra revealed a single deep-level trap with the energy position in the band gap at ~0.35 eV, i.e., very close to the values previously reported for sulfur vacancies[19,22,26]. More recently, Ci et al. have also reported results on DLTS and the current transient spectroscopic (CTS) studies of deep levels in exfoliated multilayer MoS_2, WS_2 and their alloys, such as $Mo_{1-x}W_xS_2$[25]. For MoS_2 the authors found two DLTS peaks of majority carrier traps at ~0.3 eV and ~0.4 eV. By combining the DLTS/CTS results with DFT calculations and STEM imaging or photoconductivity measurements the authors were able to identify one trap as V_S and another as a metastable DX center[25].

Table 1. Lattice constants, dielectric constants, and band gaps of TMDs.

a, c in ÅE_g in eV	MoS_2	$MoSe_2$	$MoTe_2$	WS_2	WSe_2	WTe_2
a	3.17	3.30	3.54	3.17	3.30	3.54
c	12.4	13.0	14.1	12.4	13.1	14.1
$\varepsilon_\perp$	6.56	7.92	10.7	6.10	7.46	9.80
$\varepsilon_\parallel$	15.3	16.9	20.2	13.9	15.4	18.9
$E_{g,bulk}$ (rev-vdW-DF2)	0.86	0.82	0.69	0.98	0.93	0.65
$E_{g,bulk}$ (HSE06)	1.23	1.09	1.00	1.35	1.20	0.97
$E_{g,bulk}$ (Exp)[70,71]	1.23	1.09	1.00	1.35	1.20	-
$E_{g,2D}$ (rev-vdW-DF2)	1.65	1.38	0.97	1.61	1.28	0.77
$E_{g,2D}$ (HSE06)	1.90	1.57	1.10	2.01	1.63	1.15
$E_{g,2D}$ (Exp)[72–75]	1.87–1.92	1.52–1.58	1.10	1.98–2.05	1.62–1.66	1.15

Lattice constants (a and c), dielectric constants ($\varepsilon_\perp$ and $\varepsilon_\parallel$), band gaps (E_g) calculated using rev-vdW-DF2; band gaps obtained from the HSE06 calculations; and previously reported experimental band gaps (Exp). The bulk lattice and dielectric constants were used for 2D calculations as well.

In this work, we study the charge transition levels of native point defects in 2H-MX_2 (M = Mo or W; X = S, Se, or Te) experimentally and computationally in a consistent fashion. By combining state-of-the-art computational methods (which include selection of functional, electrostatic correction, and band alignment), we establish an accurate method of predicting charge transition levels of native defects in the bulk MX_2. Simultaneously, we experimentally measure the defect levels using DLTS, which is a high-frequency capacitance transient technique, considered as a direct and accurate way to measure the charge transition levels of defects in semiconductors[41]. Finally, with the use of the computational methods verified by the DLTS experiments for the bulk TMDs, we predict the charge transition levels of native defects in the 2D MX_2 and compare the results with the calculated charge transition levels for the bulk systems.

RESULTS AND DISCUSSION

Computational prediction of defect levels in bulk TMDs

Our successful prediction of the charge transition levels is attributed to the combination of state-of-the-art computational methods: (1) the proper selection of functionals, (2) the electrostatic correction, and (3) the band alignment. In order to find a functional that best describes the six TMD systems, we tested the following functionals: PBE + D3[42], SCAN + rVV10[43], rev-vdW-DF2[44], PBE + rVV10L[45], PBEsol+rVV10s[46], optB88-vdW[47], vdW-DF-cx[48], and Heyd, Scuseria, and Ernzerhof (HSE06)[49]. Since vdW interactions play a key role in establishing the interplanar separation in bulk TMDs, it was expected that functionals that can describe those interactions correctly would perform best. The lattice constants of the six TMDs calculated with rev-vdW-DF2 agree the best with the previously reported experimental lattice constants[33,50–55] and are tabulated along with dielectric constants and band gaps in Table 1. Although SCAN + rVV10 has yielded accurate results along with rev-vdW-DF2[33] and has been used to study the charge transition levels of defects in MoS_2[28], when it comes to the prediction of the experimental lattice constants of the six TMDs studied here, we found that rev-vdW-DF2 (mean absolute error (MAE): 0.49 %) is slightly better than SCAN + rVV10 (MAE: 0.64 %). The lattice constants calculated using the other functionals are shown in Supplementary Table 1. As expected, the rev-vdW-DF2 calculations underestimated the band gaps. The hybrid HSE06 functional was used for band gap calculations, as it is regarded as the most suitable for calculating band gaps. To allow for the most accurate comparison with our experimental measurements, the fraction of exact exchange used in HSE06 was adjusted to precisely reproduce the experimentally observed values of the band gaps. The fractions of the exact exchange used in this work are 0.16 (MoS_2), 0.13 ($MoSe_2$), 0.25 ($MoTe_2$), 0.187 (WS_2), 0.18 (WSe_2), and 0.18 (WTe_2). For WTe_2, we used a value that was calculated as an average of the five other systems, since the experimental band gap of 2H-WTe_2 is not known.

The electrostatic interaction of the defect with its periodic images was corrected using the correction scheme developed by Freysoldt et al.[31,32], which has been considered the best to date[56]. Recently, the scheme developed by Freysoldt et al. has been extended to be able to correct the electrostatic interactions in 2D systems and it has been applied to 2D MoS_2[28]. Because of the documented performance of this scheme and the fact that it allows for the correction of the electrostatic interaction consistently both in bulk and 2D TMDs, we adopted this scheme to study the charge transition levels of defects in this work.

Next, the underestimation of the band gap caused by the use of a semi-local rev-vdW-DF2 functional was remedied by applying a modified band alignment method[57], which is modification of the conventional band alignment method[58]. In this approach, the position of charge transition level as well as the VBM and the CBM are shifted based on the relative positions of band edges calculated with semi-local and hybrid functionals, with an additional band gap-dependent correction. The computationally determined charge transition levels calculated with the different band alignment methods are tabulated in Supplementary Table 2 for all levels found experimentally in our current study. Overall, as expected, the modified band alignment provides best matches for the charge transition levels found in our experiments.

The formation energies of intrinsic point defects in the six bulk TMDs calculated at the chalcogen-rich condition are shown in Fig. 1. The corresponding energies for metal-rich conditions are shown in Supplementary Fig. 1. It has been reported that the most stable defect in MoS_2 is sulfur vacancy[27]. The same qualitative trend is found in our results not only of MoS_2 but also for the other systems, where the chalcogen vacancy is the defect with the lowest formation energy. In Fig. 1 we show the charge transition levels of intrinsic point defects in the six bulk TMDs considered in our study. In Table 2, we tabulate these levels as referenced to the CBM, since these are the quantities that are directly comparable to the values measured by DLTS. In the case of the chalcogen vacancy, only the 0/−1 transitions were found to be inside the band gap in the bulk systems. Note that all the 0/−1 transitions were found close to the CBM. In addition, we found that the location of the 0/−1 transition with respect to the CBM is virtually unaffected by the selection of the metal (M = Mo, W): MS_2 (0.34–0.36 eV below the CBM), MSe_2 (0.12–0.13 eV below the CBM), and MTe_2 (0.22 eV below the CBM). The metal vacancy, found to be the second most stable

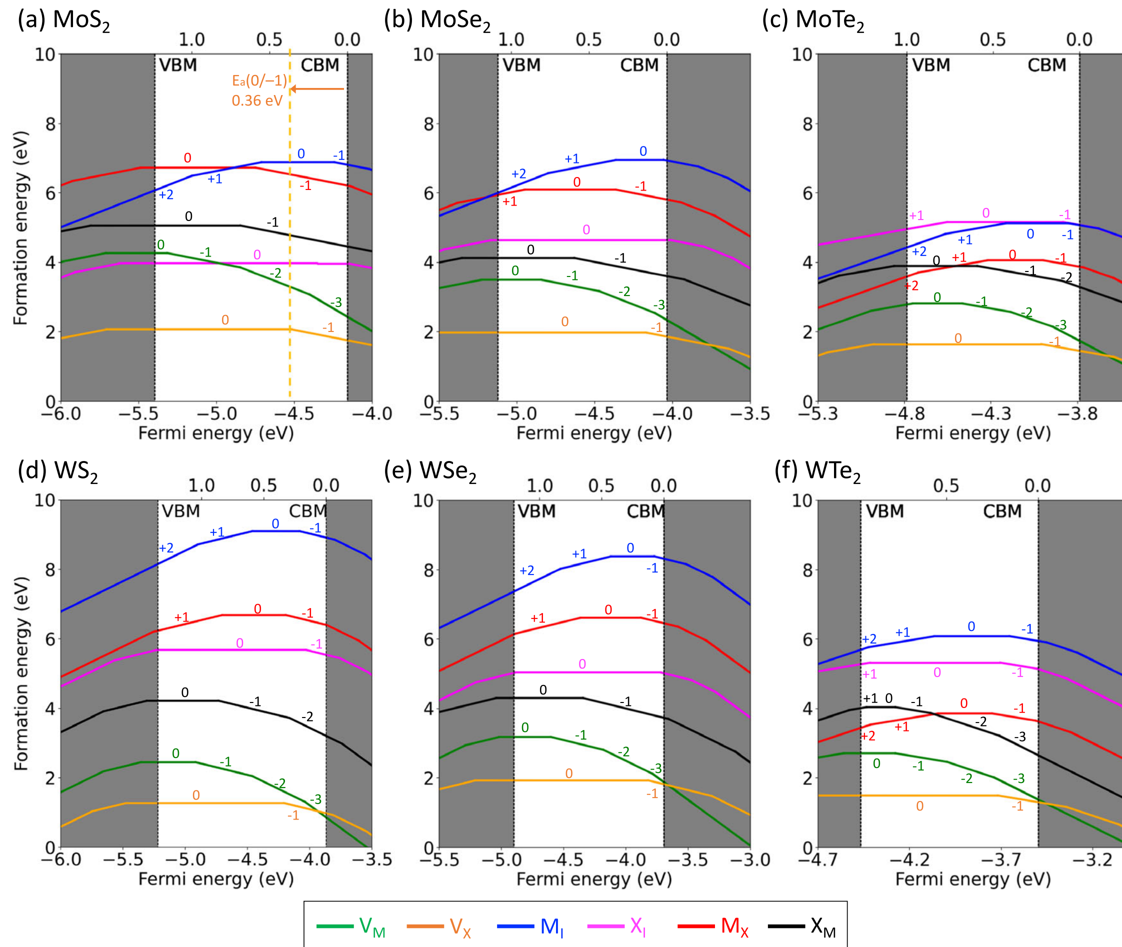

Fig. 1 Defect formation energies of point defects in bulk TMDs. The defect formation energies calculated at the chalcogen-rich condition as a function of Fermi energy in bulk (**a**) MoS_2, (**b**) $MoSe_2$, (**c**) $MoTe_2$, (**d**) WS_2, (**e**) WSe_2, and (**f**) WTe_2.

over the broad range of Fermi energies in each of the six systems, has three charge transition levels inside the band gap: 0/−1, −1/−2, and −2/−3 in all the systems. None of the charge transition levels of chalcogen interstitial were found inside the band gap in MoS_2, $MoSe_2$, and WSe_2.

Experimental determination of defect levels in bulk TMDs

To complement the theoretically predicted charge transitions levels, high quality synthetic TMD bulk crystals (2H phases) have been studied with DLTS. Only WTe_2 was not considered for further electrical experiments, because the crystal exhibited native semi-metallic properties with the typical charge carrier density ~10^{20} cm^{-3} [55,59], . All other crystals were *n*-type semiconductors, and their Schottky barrier devices were fabricated (see Methods) in order to perform DLTS experiments. The quality of the Schottky diodes has been initially checked by temperature-dependent current-voltage (*I–V*) and capacitance–voltage (*C–V*) characteristics (Supplementary Fig. 4). The main properties of the studied TMD bulk crystals are summarized in Supplementary Table 4.

Representative examples of *I–V* curves of the five TMD-based devices recorded at 300 K are shown in Fig. 2. The measurements were performed for voltage ranging from −3 V to +2 V and for the current limit of 10 mA. The results confirm the presence of Schottky-ohmic contacts with *n*-type conductivity for MoS_2, WS_2, $MoSe_2$, and Wse_2. Only $MoTe_2$ exhibited high current flow in both directions, indicating ohmic-ohmic behavior, which is due to the very high carrier concentration in the material, far above 10^{17} cm^{-3} (see Supplementary Table 4). At the end, after rejection of $MoTe_2$ (ohmic properties) and WTe_2 (semi-metallic) the remaining MX_2 showed reasonable rectifying properties, which makes them fully amenable to further studies of deep-level defects by means of a space-charge technique, such as DLTS. As the studied samples are *n*-type, the detected defects are deep donors.

Figure 3a–d shows standard DLTS temperature spectra of MoS_2, WS_2, $MoSe_2$, and WSe_2. As illustrated in Fig. 3, single positive peaks dominate the DLTS spectra of MoS_2 and WS_2. These peaks are labeled A1 and B1, respectively. Their activation energies are very close to each other, indicating the same origin of both traps. On the other hand, at least three overlapping peaks, labeled C1-C3 and D1-D3, were revealed in $MoSe_2$ and WSe_2. In order to clearly determine the accurate number of peaks composing the DLTS signal, we used standard curve fitting procedure of multiple peaks with a Gaussian function (marked with colored solid lines in Fig. 3).

There have been a number of previously reported theoretical studies on the charge transition levels in TMDs[10–14,26–29]. The charge transition level of V_S (0/−1) in bulk MoS_2 referenced to the vacuum obtained from the previous studies are ~−4.75 eV and −4.77 eV[27] and −4.6 eV[28]. The same values referenced to CBM, as is most convenient for purposes of comparison with the DLTS results, are 0.31 eV and 0.77 eV[27] and 0.28–0.38 eV[28]. The authors of Reference[27] note that they arrive at two very different values due to the use of two different calculation methods. These two values curiously coincide with experimental studies where a deep donor level was found at about 0.27 eV below the CBM in MoS_2/graphene heterojunction transistors using the

Table 2. Charge transition levels of defects identified in Fig. 1.

Defect	MoS_2	$MoSe_2$	$MoTe_2$	WS_2	WSe_2	WTe_2
V_M	1.16 (0/−1) 0.69 (−1/−2) 0.24 (−2/−3)	0.8 (0/−1) 0.44 (−1/−2) 0.08 (−2/−3)	0.68 (0/−1) 0.40 (−1/−2) 0.15 (−2/−3)	1.05 (0/−1) 0.59 (−1/−2) 0.17 (−2/−3)	0.91 (0/−1) 0.49 (−1/−2) 0.09 (−2/−3)	0.78 (0/−1) 0.50 (−1/−2) 0.24 (−2/−3)
V_X	0.36 (0/−1)	0.13 (0/−1)	0.22 (0/−1)	0.34 (0/−1)	0.12 (0/−1)	0.22 (0/−1)
M_I	1.0 (+2/+1) 0.55 (+1/0) 0.08 (0/−1)	0.76 (+2/+1) 0.33 (+1/0)	0.78 (+2/+1) 0.43 (+1/0) 0.06 (0/−1)	1.03 (+2/+1) 0.59 (+1/0) 0.21 (0/−1)	0.83 (+2/+1) 0.43 (+1/0) 0.08 (0/−1)	0.93 (+2/+1) 0.57 (+1/0) 0.15 (0/−1)
X_I	None	None	0.77 (+1/0) 0.09 (0/−1)	0.16 (0/−1)	None	0.92 (+1/0) 0.21 (0/−1)
M_X	0.59 (0/−1)	0.91 (+1/0) 0.33 (0/−1)	0.93 (+2/+1) 0.53 (+1/0) 0.21 (0/−1)	0.84 (+1/0) 0.32 (0/−1)	0.67 (+1/0) 0.18 (0/−1)	0.92 (+2/+1) 0.55 (+1/0) 0.25 (0/−1)
X_M	0.68 (0/−1)	0.59 (0/−1)	0.59 (0/−1) 0.10 (−1/−2)	0.86 (0/−1) 0.29 (−1/−2)	0.65 (0/−1)	0.94 (+1/0) 0.78 (0/−1) 0.60 (−1/−2) 0.21 (−2/−3)

The levels are referenced to the CBM.

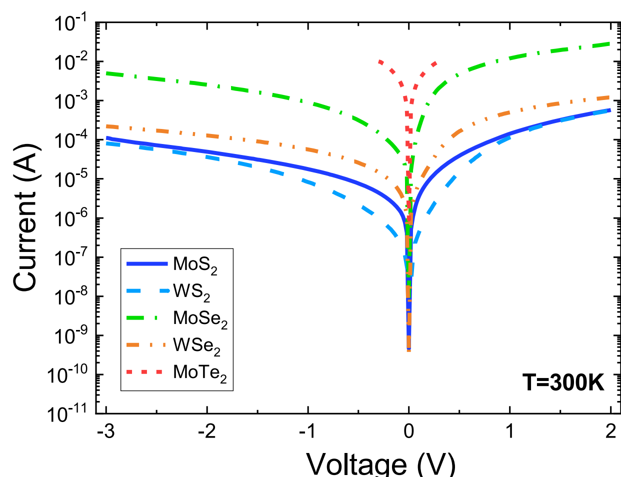

Fig. 2 The I-V characteristics for different bulk TMDs. The measurements were performed at 300 K under identical bias conditions, i.e., from −3 V to +2 V range and 10 mA current limit.

temperature-dependent *I*–*V* measurement[23], whereas combination of STM and STS methods have revealed a donor level in bulk MoS_2 at 0.7 eV below the CBM[15]. This suggests that a certain level of ambiguity is still present in both theoretical and experimental literature. Our result of −4.53 eV and 0.36 for V_S (0/−1) for the charge transition level referenced to vacuum and CBM, respectively, generally agree with the values from Reference[28] and one of the approaches used in Reference[27], although in this work we paid particular attention to account for the experimental value of the band gaps and therefore expect higher reliability of the obtained values than from other methods. A more convincing argument for the accuracy of our calculation is presented further in this paragraph, where we compare them to our DLTS experiments and find a very good agreement.

Only a few of the previously calculated defects were confirmed experimentally[19–25]. Because of its popularity, most of the experimental evidence has focused on the native point defects in MoS_2[19,23–25] and much less has been devoted to examining defects in other TMDs, such as WSe_2[20] or WS_2[21,22]. Moreover, in most cases the reported charge transition levels of defects were obtained from indirect measurements, such as PL[19–22], *I*–*V*[23] or STS[15], with two exceptions of direct studies performed by DLTS[24,25].

Defect-related PL spectra can provide important complementary data for DLTS measurements and DFT calculations. However, only the monolayer TMDs with the direct band gap are suitable for PL spectroscopy to detect radiative defects. Moreover, TMDs samples are additionally irradiated with fast particles or argon plasma, in order to increase the sensitivity of PL bands to defect-related emissions, i.e., emissions lower than band-to-band optical transitions associated with excitons bound to defects. For instance, in the low-temperature PL spectra of *α*-particle irradiated MoS_2, Tongay et al.[19] reported defect-induced PL emission peak at ~1.78 eV (i.e., ~0.12 eV below CBM), which they attributed to theoretically predicted discrete energy levels at ~0.2–0.3 eV near the VBM/CBM introduced by V_S. Room-temperature PL emission was also observed at ~1.90 (i.e., ~0.11 eV below CBM) in WS_2 monolayers through plasma treatment[22], as well as in pristine WS_2 monolayers at ~1.88 eV (i.e., ~0.15 eV below CBM)[21]. Two defect-activated PL emission peaks located at ~1.60 eV and 1.35 eV (i.e., ~0.13 eV and ~0.38 eV below CBM) were also observed by Wu et al.[20] in the low-temperature PL spectra of monolayer WSe_2 treated with Ar^+ plasma. The observed emissions were attributed by the authors to the recombination of excitons bound to different types of native defects, such as metal vacancies or their clusters, or antisite defects in WSe_2 monolayer. In line with the results presented above, it can be seen that the PL estimated charge transition levels of defects are very diversified and it is difficult to unambiguously assign the obtained energies of PL emissions to specific defect states.

Finally, DLTS and CTS techniques were successfully used for direct probing of deep-level defects in TMDs. By using standard DLTS temperature spectra we found and attributed a single deep level at 0.36 eV in bulk MoS_2 crystal (~200 µm) to native sulfur vacancies[24]. Another work, performed by Ci et al.[25], also revealed a single deep energy level below the CBM in the range of 0.25–0.31 eV in mechanically exfoliated, multilayer (~50 nm) flakes of $Mo_{1-x}W_xS_2$ ($x = 0$, 0.4, 0.7, 1). The energy positions of the deep level measured by DLTS and CTS in different samples agree well with the previous DFT calculated V_S levels[26–28], which was found by the authors to follow the CBM of the host material. The authors found also another deep-level defect at about 0.4–0.47 eV in a few

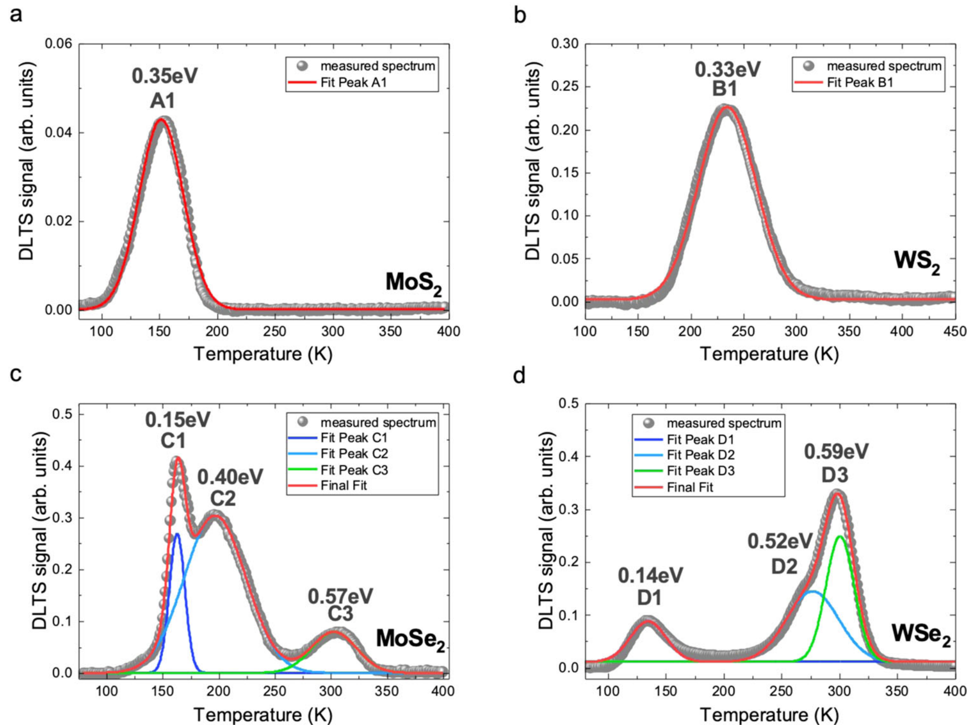

Fig. 3 Standard DLTS temperature spectra. a MoS_2, **b** WS_2, **c** $MoSe_2$, and **d** WSe_2. All the spectra were recorded with the rate window (*RW*) of 50 s-1, reverse bias (*VR*) of −1 V, filling pulse (*VP*) of 0 V and the width of the filling pulse (*tp*) of 1 ms. The solid lines represent the individual peak contribution obtained by separated Gaussian fitting. The obtained energy positions of the transition levels from the traps A, B, C and D in relation to CBM are also included in **a**–**d**.

of the studied samples, which exhibits DX center — like behavior and whose energy level lines up at a fixed position with respect to the vacuum level, explaining the observed persistent conductivity above 400 K[25].

As explained above, most of the previous studies considered only chalcogen vacancies when establishing the origin of the defect-related properties measured by different experimental methods. Moreover, most of the experimental values given in the previous studies were obtained with methods that do not directly measure the charge transition levels of defects and therefore there is still lack of reliable data to directly verify the computational results. Therefore, direct and accurate experimental determination of the position of charge transition levels, performed consistently across the entire family of TMDs, would be of great value. In this work, our computational predictions of charge transition levels agree very well with our DLTS results, which validates our computational approach and provides understanding of the origin of the DLTS results.

Table 3. Comparison between the theoretically predicted and experimentally verified charge transition levels of native point defects in bulk TMDs.

eV	Transition level (DFT)	Transition level (DLTS)	Defect origin
MoS_2	0.36	0.35	V_S (0/−1)
$MoSe_2$	0.13	0.15	V_{Se} (0/−1)
	0.44	0.40	V_{Mo} (−1/−2)
	0.59	0.57	Se_{Mo} (0/−1)
WS_2	0.34	0.33	V_S (0/−1)
WSe_2	0.12	0.14	V_{Se} (0/−1)
	0.49	0.52	V_W (−1/−2)
	0.65	0.59	Se_W (0/−1)

The corresponding defect origins identified by DFT calculations are provided. The energy values are referenced to the CBM.

Experimental verification of the computational prediction

Comparison of data in Table 2 and Fig. 3 reveals that our calculations predict the DLTS results quite well. Specifically, in MoS_2, the DLTS signal labeled A1 found at 0.35 eV below the CBM (Fig. 3a) clearly corresponds to the charge transition level of V_S (0/−1), computationally found at 0.36 eV below the CBM. Also, this result agrees well with a previous DFT study[27]. In WS_2, a single DLTS peak B1 was found with the activation energy of 0.33 eV (Fig. 3b), which again agrees well with the charge transition level of V_S (0/−1) found in our calculations at 0.34 eV below the CBM. For $MoSe_2$ and WSe_2, three deep levels were found experimentally. As shown in Fig. 3c, the DLTS signals C1 (0.15 eV), C2 (0.40 eV), and C3 (0.57 eV) found in $MoSe_2$ are likely originating from V_{Se} (0/−1), V_{Mo} (−1/−2), and Se_{Mo} (0/−1) with the levels of 0.13 eV, 0.44 eV, and 0.59 eV, respectively. Similarly, for WSe_2 the DLTS spectrum revealed three peaks, labeled D1 (0.14 eV), D2 (0.52 eV), and D3 (0.59 eV) as shown in Fig. 3d. These peaks correspond, respectively, to the computationally found charge transition levels of V_{Se} (0/−1), V_W (−1/−2), and Se_W (0/−1), positioned at 0.12 eV, 0.49 eV, and 0.65 eV below the CBM.

It is worth noting that some of the native defects are not observed in DLTS measurements but in general such defects are expected in TMD samples. The activation energies for these defects obtained in the DFT calculations should be very reliable considering the agreement between the experiment and the calculations for those that were observed experimentally. Such defects can be observed for TMDs obtained under different growth conditions or samples bombarded with alpha particles.

The summary of our experimental and computational results is shown in Table 3. In our DLTS experiments, we measured the charge transition levels of defects in MX_2 (M = Mo or W; X = S or

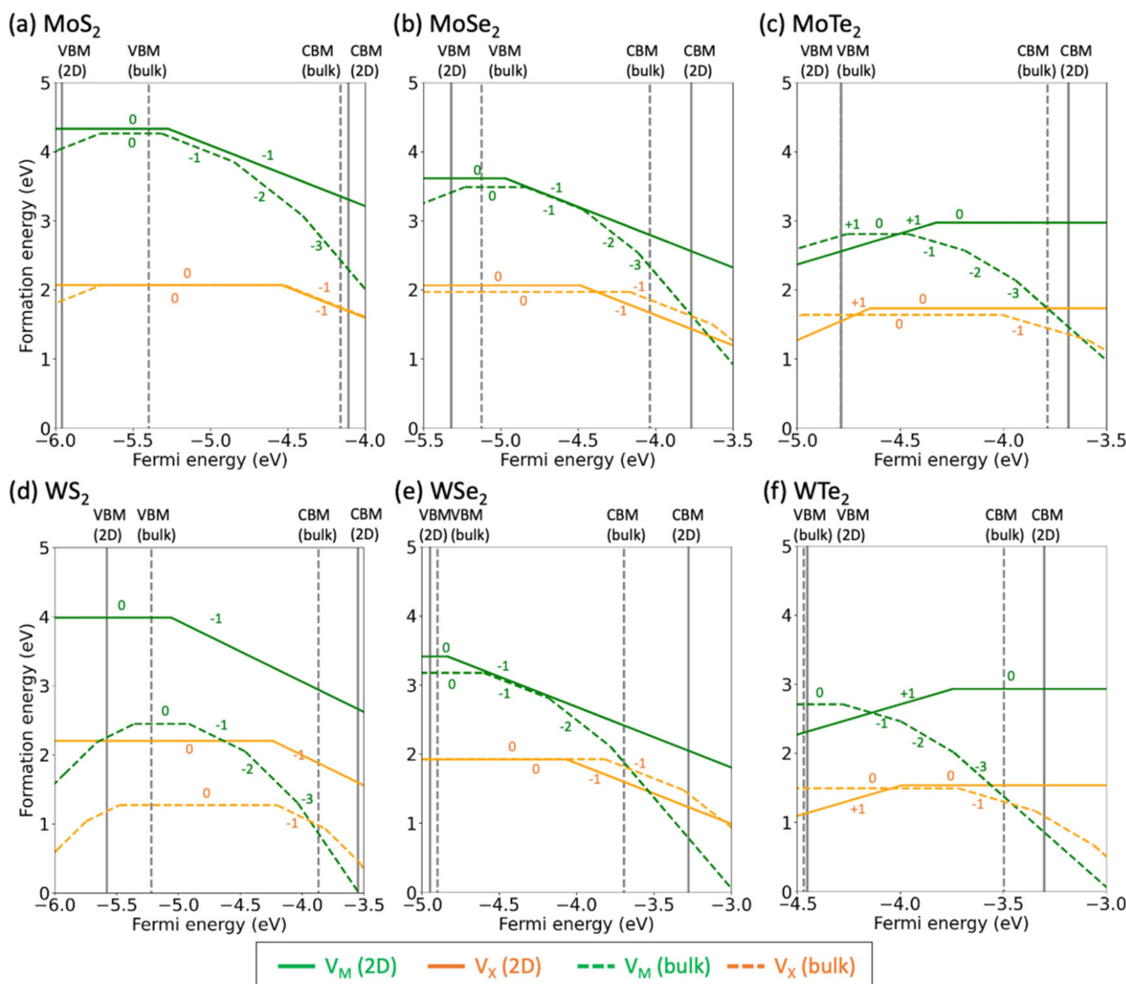

Fig. 4 Defect formation energies of metal and chalcogen vacancies in 2D (solid) and bulk (dashed) TMDs. The energies for (**a**) MoS_2, (**b**) $MoSe_2$, (**c**) $MoTe_2$, (**d**) WS_2, (**e**) WSe_2, and (**f**) WTe_2 were calculated at the chalcogen-rich condition as a function of Fermi energy.

Table 4. Identified charge transition levels of defects from Fig. 4.

Defect	MoS_2	$MoSe_2$	$MoTe_2$	WS_2	WSe_2	WTe_2
V_M	1.16 (0/−1)	1.20 (0/−1)	0.66 (+1/0)	1.51 (0/−1)	1.56 (0/−1)	0.44 (+1/0)
V_X	0.43 (0/−1)	0.64 (0/−1)	0.96 (+1/0)	0.69 (0/−1)	0.79 (0/−1)	0.66 (+1/0)

The levels are referenced to the CBM.

Se), which agree well with our DFT calculations. The good agreement between our computational prediction and the results obtained from DLTS, a direct and accurate experimental method of determining defect levels, suggests a high reliability of our computational approach. We now use the same computational strategy just validated on the bulk TMDs to predict defect properties in 2D TMDs, which cannot be measured with DLTS due to lack of a depletion layer in 2D TMDs.

Computational prediction of defect levels in 2D TMDs

In Fig. 4, we plotted the formation energies of vacancies (metal and chalcogen) in the six 2D MX_2 (solid) and bulk MX_2 (dashed) calculated using the DLTS-verified method at the chalcogen-rich condition. In Table 4, we tabulated the charge transition levels of vacancies in the six 2D MX_2 identified from Fig. 4. For the metal and chalcogen vacancies, the only type of transition found inside the band gaps is 0/−1 in MoS_2, $MoSe_2$, WS_2, and WSe_2, whereas in $MoTe_2$ and WTe_2 the only transition found inside the band gaps is +1/0. For MoS_2, our results are in a good agreement with earlier computational studies. Specifically, Tan et al.[28] reported the charge transition levels of V_S in bulk and 2D MoS_2, which are ~ −4.6 eV and −4.5 eV referenced to the vacuum level, respectively (read off the plot in ref. [28]). The aforementioned values agree well with our results, which are −4.53 eV and −4.52 eV for V_S in bulk and 2D MoS_2, respectively.

It is instructive to compare the calculated charge transition levels of defects in the bulk and 2D TMDs. First of all, we found that, unlike the bulk systems where the metal vacancies have many transition levels inside their band gaps, in the 2D systems the metal vacancies create only a single transition level inside the band gap. Secondly, previous computational studies by Komsa et al.[27] and Tan et al.[28] reported that the charge transition level of V_S is similar in bulk and 2D MoS_2, but the study was carried out

only for MoS_2. Our calculations agree with their results (the charge transition level of V_S in both bulk and 2D MoS_2 is around −4.5 eV, referenced to the vacuum level), and we also found the same trend from V_S in WS_2 (−4.20 eV for the bulk and −4.24 eV for the 2D). However, we found that this conclusion is not general as the agreement between bulk and 2D transition levels is not found in MSe_2 and MTe_2 (Fig. 4).

Data shown in Fig. 4 and Table 4 clearly demonstrates that the reduction of the dimensionality of TMDs crystals from bulk to 2D has a significant impact on both the formation energies and charge transition levels of native defects in relation to the vacuum level as well as in relation to the band gap. Although the exact reason for why fewer defect levels are present within the band gap of 2D systems as compared to their bulk counterparts is not explicitly apparent from the calculations, a simple explanation is possible. In both bulk and monolayer systems, a single electron localized on a vacancy results in a charge state transition level within the band gap. However, a vacancy in a monolayer localizes electrons more strongly than in a bulk, because of the potential of the vacuum outside, resulting in a weaker screening in a monolayer than in a bulk. Therefore, when a second electron is present in a monolayer, the strong attraction between the second electron and the vacancy would localize the two electrons very close to each other, close enough for the Coulomb interaction to influence the energy of the system to be unfavorable for such a situation. That in turn means that a second charge state transition level is unlikely to be present within the band gap of the monolayer. The significant differences in formation energies and charge transition levels of the same type of defects in bulk and 2D TMDs may explain why epitaxially grown samples (i.e., grown as 2D material) and samples exfoliated from bulk crystals (i.e., 2D material obtained from a sample grown as bulk) exhibit different optical properties, with the former usually exhibiting worse optical and electrical properties[22,60,61].

In this paper, we reported charge transition levels of native defects in MX_2 (M = Mo or W; X = S, Se, or Te) using state-of-the-art computational methods, including DFT calculations with the optimized functional, electrostatic correction, and band alignment. We also measured the defect levels directly by means of DLTS experiments, which agreed well with the computational predictions. We found that the chalcogen vacancy, the most stable defect in each of the six bulk MX_2, creates the 0/−1 charge transition inside the band gap and that the selection of transition metal has only little effect on the position of the 0/−1 charge transition. The very good agreement of experimental and computational results validated the computational approach and allowed for identification of the origin of experientially found defect levels. The same computational approach has been then used to calculate the charge transition levels of defects in 2D MX_2. Our computational results shed light on the defect properties in 2D MX_2, which is experimentally not feasible. In addition, by comparing the bulk and 2D TMDs data, we found significant differences in trends of the charge transition levels of defects in the bulk and 2D TMDs. This joint computational and experimental work provides validated and consistent data regarding the charge transition levels of defects in bulk and 2D MX_2 and their chemical trends and also lays out a relatively inexpensive computational strategy for accurately determining the charge transition levels of defects in TMDs. This work may aid in properly designing and fabricating TMD-based applications.

METHODS

Sample preparation

The bulk TMDs used in our study were commercially available vdW crystals supplied by HQ Graphene, except for MoS_2, which was obtained from 2D Semiconductors. Multilayer (~200 µm thick) MoS_2, $MoSe_2$, $MoTe_2$, WS_2, and WSe_2 have a typical lateral size of about 5 mm, parallel to the hexagonal lattice plane. For DLTS and other temperature-dependent electrical measurements, samples were mounted on a high quality (~0.8 mm thick) printed circuit board (PCB) holder with copper tracks, designed specifically for our cryostats. Gold (Au) or nickel (Ni) circular contacts (with ~0.1 mm^2 area), deposited in vacuum through shadow mask by magnetron sputtering on the top side of each sample, were used as the Schottky barrier contact, and the large area (~10–12 mm^2) Au bottom electrode was used as an ohmic contact. The ohmic contact was additionally annealed at 350 °C in argon (Ar) atmosphere to ensure nonrectifying electrical conductivity through the metal-semiconductor junction (i.e., ohmic-like behavior).

The general strategy for measuring DLTS across the sample is to make an ohmic contact on one side (the bottom contact) and a Schottky contact on the other side (the top contact) of the sample. The bottom contact is made over a large area and has an ohmic characteristic. This is because over such a large area the crystal is not atomically smooth, and it is easy to find areas where the contact is ohmic if proper metallization is used. The ohmic characteristic can be improved by annealing. The top contacts have small areas and such contacts are made in series of different diameters (0.1, 0.3, 0.5, 0.8 mm). If the top contact has an ohmic characteristic, it is not suitable for DLTS measurements. If this contact is on an atomically smooth surface and has a Schottky characteristic, it is suitable for DLTS measurements. With this approach, it is possible to fabricate Schottky diodes on bulk van der Waals crystals with the same metal for ohmic and Schottky contact for certain crystals and metals. It is worth noting that defects that could form at the m–s junction as a result of the metal deposition, are not expected to make a significant contribution to DLTS measurements. These defects typically form in 1–3 monolayers near the m–s interface and therefore do not influence the depletion layer during DLTS measurements of bulk crystal[39,40]. In this case, the depletion layer is at least two orders of magnitude thicker than the metallization-damaged layer and usually located much deeper below m–s interface, depending on the DLTS bias conditions. This situation is analogous to DLTS measurements on common bulk materials, such as GaAs, InP, etc[62]. Metallic impurities are known to affect various device parameters, if they are located at the semiconductor-oxide interface or in the junction space-charge regions[63]. The requirements for the formation of Schottky contacts would be different for measurements on very thin van der Waals crystals. In that case, it is recommended that one mechanically transfers metal electrode onto the surface of the vdW crystal instead of chemically deposit it.

Electrical measurements

We used a hand-made Laplace DLTS system, designed to measure electrical characteristics (i.e., LDLTS, DLTS, *I–V*, and *C–V* curves) of semiconductors in a wide temperature range. For the experiments, samples were mounted in a liquid nitrogen cooled Janis VPF-475 cryostat, where temperature is precisely tuned by Lakeshore 331 temperature controller within the range of 80 K to 480 K. High-frequency capacitance transients were measured by means of Boonton 7200 capacitance bridge, operating at frequency of 1 MHz and A.C. voltage with an amplitude of ~30 mV superimposed onto the D.C. reverse bias. In turn, the current-voltage characteristics were measured by 2601 A Keithley source measure unit (SMU) instrument.

For consistency, the DLTS measurements were performed at the same bias conditions, i.e., the steady-state small reverse bias $V_R = -1$ V and the filling pulse voltage (V_P), which reduces the reverse bias to 0 V and allows the traps to be filled with free electrons. Considering such bias conditions and free carrier concentration at ~10^{16} cm^{-3} in the DLTS measured TMDs samples

(Supplementary Table 4), the minimum depth in the depletion region that can be sampled at zero bias is equal to about 0.2 µm, while −1 V reverse bias is equivalent to a depletion depth of about 0.4 µm. Next, the capacitance transients related to the emission of majority carriers from the deep-level traps in the depletion region were recorded. The width of the filling pulse (t_P) was set to 1 ms and the emission rate window (*RW*) was equal to 50 s^{-1}. For such measurement conditions, the capacitance difference within the specified *RW* (i.e., DLTS signal) reaches the maximum at a specific temperature. In our DLTS system, a positive signal indicates that all the visible peaks correspond to the majority carrier traps with the energy levels measured from the CBM.

The energy position (E_T) of a charge transition level in relation to the CBM (E_C), called activation energy ($E_a = E_C - E_T$), and the apparent capture cross-section (σ_n) can be determined on the basis of the detailed balance equation[41,64]:

$$e_n = \sigma_n V_{th} N_C \exp\left(\frac{E_C - E_T}{k_B T}\right) \quad (1)$$

where e_n stands for the thermal emission rate for electrons from a deep-level into the conduction band at temperature T, v_{th} is the thermal velocity of the electrsons, N_C is the effective density of states in the conduction band and k_B is the Boltzmann's constant. Considering that $v_{th} \propto T^{1/2}$ and $N_C \propto T^{3/2}$ and assuming the temperature independence of the capture cross section, Eq. (1) becomes a linear equation in the $\ln(e_{n,p}/T^2)$ vs $1/T$ coordinate:

$$\ln\left(\frac{e_n}{T^2}\right) = \left(\frac{E_C - E_T}{k_B}\right)\frac{1}{T} + \ln(K\sigma_n) \quad (2)$$

where K is a known constant dependent on the electron effective mass. In the standard approach, this type of Arrhenius equation can be plotted by measuring a shift in the DLTS temperature peak position as a function of a thermal emission rate. Therefore, to construct the Arrhenius plots and to calculate the parameters of deep-level defects, the DLTS temperature spectra were measured for different rate windows in the range of 5–2000 s^{-1} under the same bias conditions (Supplementary Figs. 2 and 3). Ultimately, according to Eq. (2), and from the slope of the Arrhenius plot one can obtain the activation energy of a deep-level defect, while its capture cross section is obtained from the intercept with the ordinate axis.

DFT calculations

We performed the DFT calculations using the Vienna Ab-initio Simulation Package (VASP)[65] with the projector augmented wave method[66]. To optimize the geometry of the six TMDs, different functionals were tested to find the one that most accurately describes the experimental lattice constants of the six TMDs. The tested functionals were PBE+D3[42], SCAN+rVV10[43], rev-vdW-DF2[44], PBE + rVV10L[45], PBEsol + rVV10s[46], optB88-vdW[47], and vdW-DF-cx[48]. We set the plane-wave cutoff energy of 500 eV and Γ-centered Monkhorst-Pack *k*-point mesh of $10 \times 10 \times 2$ with an energy tolerance of 1 meV/atom[67]. From the test of the different functionals, rev-vdW-DF2 was shown to exhibit the smallest error as compared to experimentally determined values and, therefore, was selected as the functional of choice for geometry optimization and total energy calculations. Due to the well-known band gap underestimation problem, for the band structures, we also performed hybrid functional calculations using Heyd, Scuseria, and Ernzerhof (HSE06)[49] with the fraction of exact exchange adjusted such that the calculated band gap agreed with the experimental band gap. The total energies of pure systems and defective systems were calculated in $5 \times 5 \times 1$ supercells with $2 \times 2 \times 2$ *k*-point mesh. Spin orbit coupling was included for all calculations in this work. For the calculations of charge transition levels of bulk systems referenced to vacuum, 12 atomic layer thick slabs were calculated alongside bulk systems, and a macroscopic potential average method[68], where the bulk-like part of the potential of the slab is aligned to the potential of the bulk and then the vacuum potential is moved to zero, the method is described in detail in ref. [69]. For monolayer calculations, all computational methods were kept the same in order to achieve results consistent with bulk calculations, only with the k-point mesh reduced to one point in the direction perpendicular to the layer. Layers were separated by 25 Å of vacuum to prevent interactions between their periodic images. In order to obtain charge transition levels of monolayers referenced to vacuum, for monolayer calculations the eigenvalues were shifted by a value that brought the potential of the vacuum region to zero.

The formation energy, $E^f[X^q](E_F)$, of a point defect X with charge q was calculated as a function of Fermi energy E_F using the following equation,

$$E^f[X^q](E_F) = E_{tot}[X^q] - E_{tot}[\text{pure}] - \sum_i^n \mu_i + q(E_{VBM}[\text{pure}] + E_F) + E_{EC} \quad (3)$$

where E_{tot} and E_{VBM} are the total energy and the valence band maximum (VBM) from the DFT calculations, respectively, n_i is the number of atoms added or removed as a defect, μ_i is the chemical potential of the elements constituting the defect, and E_{EC} is the electrostatic correction term for the interaction of the defect with the periodic images, for which we used the scheme developed by Freysoldt et al.[31,32].

After calculating the formation energies, a modified band alignment method[57,58] was used to correctly locate the charge transition levels calculated with the rev-vdW-DF2 functional in the correct, HSE06 calculated band gap, using the following equation,

$$E^d_{MBA} = E^d + E_{shift} + \beta(E_g - E^d) \quad (4)$$

where E^d_{MBA} is the corrected charge transition level, E^d is the defect level obtained from Eq. (3), E_{shift} is the difference in the VBM between the rev-vdW-DF2 and HSE06 calculations, E_g is the HSE06 band gap, and β is –0.14 as determined by Polak et al.[57].

DATA AVAILABILITY

All data used in this study are available from the corresponding authors upon reasonable request.

Received: 7 December 2021; Accepted: 30 September 2022;
Published online: 29 October 2022

REFERENCES

1. Splendiani, A. et al. Emerging photoluminescence in monolayer MoS_2. *Nano Lett.* **10**, 1271–1275 (2010).
2. Radisavljevic, B., Radenovic, A., Brivio, J., Giacometti, V. & Kis, A. Single-layer MoS_2 transistors. *Nat. Nanotechnol.* **6**, 147–150 (2011).
3. Choi, W. et al. Recent development of two-dimensional transition metal dichalcogenides and their applications. *Mater. Today* **20**, 116–130 (2017).
4. Das, S., Chen, H. Y., Penumatcha, A. V. & Appenzeller, J. High performance multilayer MoS_2 transistors with scandium contacts. *Nano Lett.* **13**, 100–105 (2013).
5. Lee, G. H. et al. Flexible and transparent MoS_2 field-effect transistors on hexagonal boron nitride-graphene heterostructures. *ACS Nano* **7**, 7931–7936 (2013).
6. Geim, A. K. & Grigorieva, I. V. Van der Waals heterostructures. *Nature* **499**, 419–425 (2013).
7. Li, M. Y., Chen, C. H., Shi, Y. & Li, L. J. Heterostructures based on two-dimensional layered materials and their potential applications. *Mater. Today* **19**, 322–335 (2016).
8. Velický, M. & Toth, P. S. From two-dimensional materials to their heterostructures: an electrochemist's perspective. *Appl. Mater. Today* **8**, 68–103 (2017).
9. Liu, K. K. et al. Growth of large-area and highly crystalline MoS_2 thin layers on insulating substrates. *Nano Lett.* **12**, 1538–1544 (2012).
10. Guo, Y., Liu, D. & Robertson, J. Chalcogen vacancies in monolayer transition metal dichalcogenides and Fermi level pinning at contacts. *Appl. Phys. Lett.* **106**, 173106 (2015).
11. Liu, D., Guo, Y., Fang, L. & Robertson, J. Sulfur vacancies in monolayer MoS_2 and its electrical contacts. *Appl. Phys. Lett.* **103**, 183113 (2013).

12. McDonnell, S., Addou, R., Buie, C., Wallace, R. M. & Hinkle, C. L. Defect-dominated doping and contact resistance in MoS_2. *ACS Nano* **8**, 2880–2888 (2014).
13. Qiu, H. et al. Hopping transport through defect-induced localized states in molybdenum disulphide. *Nat. Commun.* **4**, 1–6 (2013).
14. Hong, J. et al. Exploring atomic defects in molybdenum disulphide monolayers. *Nat. Commun.* **6**, 1–8 (2015).
15. Lu, C. P., Li, G., Mao, J., Wang, L. M. & Andrei, E. Y. Bandgap, mid-gap states, and gating effects in MoS_2. *Nano Lett.* **14**, 4628–4633 (2014).
16. Vancsó, P. et al. The intrinsic defect structure of exfoliated MoS_2 single layers revealed by scanning tunneling microscopy. *Sci. Rep.* **6**, 1–7 (2016).
17. Barja, S. et al. Identifying substitutional oxygen as a prolific point defect in monolayer transition metal dichalcogenides. *Nat. Commun.* **10**, 1–8 (2019).
18. Wu, Z. & Ni, Z. Spectroscopic investigation of defects in two-dimensional materials. *Nanophotonics* **6**, 1219–1237 (2017).
19. Tongay, S. et al. Defects activated photoluminescence in two-dimensional semiconductors: interplay between bound, charged, and free excitons. *Sci. Rep.* **3**, 2657 (2013).
20. Wu, Z. et al. Defect activated photoluminescence in WSe_2 monolayer. *J. Phys. Chem. C.* **121**, 12294–12299 (2017).
21. Chow, P. K. et al. Defect-induced photoluminescence in monolayer semiconducting transition metal dichalcogenides. *ACS Nano* **9**, 1520–1527 (2015).
22. McCreary, A. et al. Distinct photoluminescence and Raman spectroscopy signatures for identifying highly crystalline WS_2 monolayers produced by different growth methods. *J. Mater. Res.* **31**, 931–944 (2016).
23. Kwak, J. Y. et al. Electrical characteristics of multilayer MoS_2 FETs with MoS_2/graphene heterojunction contacts. *Nano Lett.* **14**, 4511–4516 (2014).
24. Gelczuk, Ł. et al. Probing defects in MoS_2 Van der Waals crystal through deep-level transient spectroscopy. *Rapid Res. Lett.* https://doi.org/10.1002/pssr.202000381 (2020).
25. Ci, P. et al. Chemical trends of deep levels in van der Waals semiconductors. *Nat. Commun.* **11**, 5373 (2020).
26. Zhou, W. et al. Intrinsic structural defects in monolayer molybdenum disulfide. *Nano Lett.* **13**, 2615–2622 (2013).
27. Komsa, H. P. & Krasheninnikov, A. V. Native defects in bulk and monolayer MoS_2 from first principles. *Phys. Rev. B* **91**, 125304 (2015).
28. Tan, A. M. Z., Freysoldt, C. & Hennig, R. G. Stability of charged sulfur vacancies in 2D and bulk MoS_2 from plane-wave density functional theory with electrostatic corrections. *Phys. Rev. Mater.* **4**, 64004 (2020).
29. Noh, J.-Y., Kim, H. & Kim, Y.-S. Stability and electronic structures of native defects in single-layer MoS_2. *Phys. Rev. B* **89**, 205417 (2014).
30. Bertoldo, F., Ali, S., Manti, S. & Thygesen, K. S. Quantum point defects in 2D materials—the QPOD database. *npj Computational Mater.* **8**, 56 (2022).
31. Freysoldt, C., Neugebauer, J. & Van De Walle, C. G. Fully Ab initio finite-size corrections for charged-defect supercell calculations. *Phys. Rev. Lett.* **102**, 016402 (2009).
32. Freysoldt, C., Neugebauer, J. & Van de Walle, C. G. Electrostatic interactions between charged defects in supercells. *Phys. Status Solidi B***248**, 1067–1076 (2011).
33. Tran, F., Kalantari, L., Traoré, B., Rocquefelte, X. & Blaha, P. Nonlocal van der Waals functionals for solids: choosing an appropriate one. *Phys. Rev. Mater.* **3**, 063602 (2019).
34. Edelberg, D. et al. Approaching the intrinsic limit in transition metal diselenides via point defect control. *Nano Lett.* **19**, 4371–4379 (2019).
35. Kim, B. et al. Free trions with near-unity quantum yield in monolayer $MoSe_2$. *ACS Nano* **16**, 140–147 (2022).
36. Wang, K. et al. Selective antisite defect formation in WS_2 monolayers via reactive growth on dilute W–Au alloy substrates. *Adv. Mater.* **34**, 2106674 (2022).
37. Allain, A., Kang, J., Banerjee, K. & Kis, A. Electrical contacts to two-dimensional semiconductors. *Nat. Mater.* **14**, 1195–1205 (2015).
38. Kim, C. et al. Fermi level pinning at electrical metal contacts of monolayer molybdenum dichalcogenides. *ACS Nano* **11**, 1588–1596 (2017).
39. Wang, Y. & Chhowalla, M. Making clean electrical contacts on 2D transition metal dichalcogenides. *Nat. Rev. Phys.* **4**, 101–112 (2022).
40. Liu, Y. et al. Approaching the Schottky–Mott limit in van der Waals metal–semiconductor junctions. *Nature* **557**, 696–700 (2018).
41. Lang, D. V. Deep-level transient spectroscopy: a new method to characterize traps in semiconductors. *J. Appl. Phys.* **45**, 3023–3032 (1974).
42. Grimme, S., Antony, J., Ehrlich, S. & Krieg, H. A consistent and accurate ab initio parametrization of density functional dispersion correction (DFT-D) for the 94 elements H-Pu. *J. Chem. Phys.* **132**, 154104 (2010).
43. Peng, H., Yang, Z. H., Perdew, J. P. & Sun, J. Versatile van der Waals density functional based on a meta-generalized gradient approximation. *Phys. Rev. X* **6**, 041005 (2016).
44. Hamada, I. Van der Waals density functional made accurate. *Phys. Rev. B* **89**, 121003 (2014).
45. Peng, H. & Perdew, J. P. Rehabilitation of the Perdew-Burke-Ernzerhof generalized gradient approximation for layered materials. *Phys. Rev. B* **95**, 081105 (2017).
46. Terentjev, A. V., Constantin, L. A. & Pitarke, J. M. Dispersion-corrected PBEsol exchange-correlation functional. *Phys. Rev. B* **98**, 214108 (2018).
47. Klimeš, J., Bowler, D. R. & Michaelides, A. Chemical accuracy for the van der Waals density functional. *J. Phys. Condens. Matter* **22**, 022201 (2010).
48. Berland, K. & Hyldgaard, P. Exchange functional that tests the robustness of the plasmon description of the van der Waals density functional. *Phys. Rev. B* **89**, 035412 (2014).
49. Perdew, J. P., Burke, K. & Ernzerhof, M. Generalized gradient approximation made simple. *Phys. Rev. Lett.* **77**, 3865–3868 (1996).
50. Wakabayashi, N., Smith, H. G. & Nicklow, R. M. Lattice dynamics of hexagonal MoS_2 studied by neutron scattering. *Phys. Rev. B* **12**, 659–663 (1975).
51. Schutte, W. J., De Boer, J. L. & Jellinek, F. Crystal structures of tungsten disulfide and diselenide. *J. Solid State Chem.* **70**, 207–209 (1987).
52. James, P. B. & Lavik, M. T. The crystal structure of $MoSe_2$. *Acta Crystallogr.* **16**, 1183–1183 (1963).
53. Puotinen, D. & Newnham, R. E. The crystal structure of $MoTe_2$. *Acta Crystallogr.* **14**, 691–692 (1961).
54. Dawson, W. G. & Bullett, D. W. Electronic structure and crystallography of $MoTe_2$ and WTe_2. *J. Phys. C: Solid State Phys.* **20**, 6159–6174 (1987).
55. Li, S. et al. Synthesis of semiconducting 2H-phase WTe_2 nanosheets with large positive magnetoresistance. *Inorg. Chem.* **59**, 11935–11939 (2020).
56. Komsa, H. P., Rantala, T. T. & Pasquarello, A. Finite-size supercell correction schemes for charged defect calculations. *Phys. Rev. B* **86**, 045112 (2012).
57. Maciej, P. P., Robert, K., Ryan, J., Izabela, S. & Dane, M. Modified band alignment method to obtain hybrid functional accuracy from standard DFT: application to defects in highly mismatched III–V:Bi alloys. *Phys. Rev. Mater.* **5**, 124601 (2021).
58. Alkauskas, A., Broqvist, P. & Pasquarello, A. Defect energy levels in density functional calculations: alignment and band gap problem. *Phys. Rev. Lett.* **101**, 046405 (2008).
59. Li, P. et al. Evidence for topological type-II Weyl semimetal WTe_2. *Nat. Commun.* **8**, 2150 (2017).
60. Jin, C. et al. On optical dipole moment and radiative recombination lifetime of excitons in WSe_2. *Adv. Funct. Mater.* **27**, 1601741 (2017).
61. Kim, J. et al. Observation of ultralong valley lifetime in WSe_2/MoS_2 heterostructures. *Sci. Adv.* **3**, 1700518 (2017).
62. E. R. Weber. *Imperfections in III/V materials. Semiconductors and Semimetals* Vol. 38 (Academic Press Inc, 1993).
63. D. K. Schroeder. *Semiconductor material and device characterization* (John Wiley&Sons Inc, 2006).
64. Blood, P. & Orton, J. W. *The Electrical Characterization of Semiconductors: Majority Carriers and Electron States* (Academic Press, London, 1992).
65. Kresse, G. & Furthmüller, J. Efficient iterative schemes for ab initio total-energy calculations using a plane-wave basis set. *Phys. Rev. B* **54**, 11169–11186 (1996).
66. Joubert, D. From ultrasoft pseudopotentials to the projector augmented-wave method. *Phys. Rev. B* **59**, 1758–1775 (1999).
67. Monkhorst, H. J. & Pack, J. D. Special points for Brillouin-zone integrations. *Phys. Rev. B* **13**, 5188–5192 (1976).
68. Moses, P. G., Miao, M., Yan, Q. & Van De Walle, C. G. Hybrid functional investigations of band gaps and band alignments for AlN, GaN, InN, and InGaN. *J. Chem. Phys.* **134**, 084703 (2011).
69. Balderschi, A., Baroni, S. & Resta, R. Band offsets in lattice-matched heterojunctions: a model and first-principles calculations for GaAs/AlAs. *Phys. Rev. Lett.* **61**, 734–737 (1988).
70. Kam, K. K. & Parkinson, B. A. Detailed photocurrent spectroscopy of the semiconducting group VIB transition metal dichalcogenides. *J. Phys. Chem.* **86**, 463–467 (1982).
71. Böker, T. et al. Band structure of MoS_2, $MoSe_2$, and $\alpha-MoTe_2$: angle-resolved photoelectron spectroscopy and ab initio calculations. *Phys. Rev. B* **64**, 235305 (2001).
72. Gusakova, J. et al. Electronic properties of bulk and monolayer TMDs: theoretical study within DFT framework (GVJ-2e method). *Phys. Status Solidi* **214**, 1700218 (2017).
73. Ye, Z. et al. Probing excitonic dark states in single-layer tungsten disulphide. *Nature* **513**, 214–218 (2014).
74. Hanbicki, A. T., Currie, M., Kioseoglou, G., Friedman, A. L. & Jonker, B. T. Measurement of high exciton binding energy in the monolayer transition-metal dichalcogenides WS_2 and WSe_2. *Solid State Commun.* **203**, 16–20 (2015).
75. Mak, K. F., Lee, C., Hone, J., Shan, J. & Heinz, T. F. Atomically thin MoS_2: a new direct-gap semiconductor. *Phys. Rev. Lett.* **105**, 136805 (2010).

ACKNOWLEDGEMENTS

R.K., L.G., and D.H. were supported by the Foundation for Polish Science through TEAM NET grant and the National Science Centre (NCN) in Poland through OPUS

Grant No. 2017/25/B/ST7/01203. J.Y.K. and I.S. gratefully acknowledge support from the Department of Energy Basic Energy Science Program (grant # DEFG02–08ER46493). D.M. and M.P.P. acknowledge support from the National Science Foundation (NSF) Cyberinfrastructure for Sustained Scientific Innovation (CSSI) (OAC-1931298). Part of the calculations have been carried out in Wroclaw Centre for Networking and Supercomputing.

AUTHOR CONTRIBUTIONS

J.Y.K. and L.G. are co-first authors. M.P.P., R.K., and I.S. conceived the study. J.Y.K. performed DFT calculations and analyzed the data, M.P.P. performed DFT calculations, L.G. performed DLTS measurements and their analysis, D.H. made electrical contacts for DLTS measurements, J.Y.K., L.G., M.P.P., R.K., and I.S. co-wrote the manuscript, D.M. provided insights into the computational approach. All authors read, revised, and approved the final manuscript.

COMPETING INTERESTS

The authors declare no competing interests.

ADDITIONAL INFORMATION

Supplementary information The online version contains supplementary material available at https://doi.org/10.1038/s41699-022-00350-4.

Correspondence and requests for materials should be addressed to Jun Young Kim, Łukasz Gelczuk, Robert Kudrawiec or Izabela Szlufarska.

Reprints and permission information is available at http://www.nature.com/reprints

Publisher's note Springer Nature remains neutral with regard to jurisdictional claims in published maps and institutional affiliations.

Open Access This article is licensed under a Creative Commons Attribution 4.0 International License, which permits use, sharing, adaptation, distribution and reproduction in any medium or format, as long as you give appropriate credit to the original author(s) and the source, provide a link to the Creative Commons license, and indicate if changes were made. The images or other third party material in this article are included in the article's Creative Commons license, unless indicated otherwise in a credit line to the material. If material is not included in the article's Creative Commons license and your intended use is not permitted by statutory regulation or exceeds the permitted use, you will need to obtain permission directly from the copyright holder. To view a copy of this license, visit http://creativecommons.org/licenses/by/4.0/.

© The Author(s) 2022